JOURNAL OF MATERIALS SCIENCE 27 (1992) 2687–2694

Laser welding of oxide dispersion-strengthened alloy MA 754

P. A. MOLIAN, Y. M. YANG, P. C. PATNAIK
Mechanical Engineering Department, Iowa State University, Ames, IA 50011, USA
Orenda Division, Hawker Siddley Canada, Gloucester, Ontario, Canada KIJ 9L8

Conventional arc-welding of MA 754, an oxide dispersion-strengthened (ODS) superalloy, poses two significant problems: agglomeration of dispersoids and weld solidification grain boundaries perpendicular to the rolled direction, both of which reduce the high-temperature creep and stress rupture properties. In the present work, laser welding of MA 754 alloy was conducted to determine the effects of a high energy density source on the microstructure and mechanical properties of a 3.2 mm thick butt joint. Tungsten-inert-gas (TIG) welding was also studied for comparison purpose. X-ray diffraction, optical microscopy and scanning electron microscopy analysis coupled with tensile, hardness and hot corrosion tests were used to evaluate the performance of weldments. Results indicated the absence of dispersoid agglomeration and superior tensile and corrosion properties of laser weldments over arc welds. The properties of laser weldments are comparable to those of wrought MA 754.

1. Introduction

Oxide dispersion strengthening (ODS) is a method that can be employed to extend the performance of high-temperature metals. By introducing a small, stable oxide dispersoid into the metal matrix, the high-temperature strength of the materials can be significantly increased. The fine dispersoids act to pin down the dislocation motion. The oxide dispersoids are also stable at higher temperatures [1], resulting in little loss of strength. In addition, the dispersoids provide excellent high-temperature oxidation and corrosion resistance.

ODS alloys can be produced by a chemical reaction process in metal systems if the number of species alloyed is limited [2]. However, in the case of complex high-temperature superalloys used for vanes, blades or combustors of gas turbines, the mechanical alloying process was found to be the most effective [3]. In this process, alloyed powders are produced in a high energy driven ball mill which facilitates continuous cold welding, work-hardening and fracturing of elemental powders and the oxide dispersoid to form a uniform powder composition; the composition of each particle is the same as that of the bulk. The powder is then consolidated by extrusion. Hot rolling followed by recrystallization heat treatment of consolidated powders eventually produces alloys with a coarse directional grain structure. The insoluble oxide and the coarse grains together provide high-temperature strength in the direction parallel to the elongated grains. The advantage of mechanical alloying is that any element or compound can be alloyed. For example, mechanical alloying permits low-melting elements such as aluminium and high-melting elements such as chromium and nickel to be alloyed with yttrium oxide (Y_2O_3) in MA 754.

Inconel alloy MA 754 is the first mechanically alloyed (MA) ODS Ni–Cr alloy, and is being used as a turbine vane alloy in advanced gas turbine engines. The nominal composition and physical properties of this alloy [4] are given in Tables I and II, respectively. MA 754 is comparable to TD–Ni (thoria-dispersed nickel) but has a non-radioactive dispersoid. The yttrium oxide provides excellent creep and rupture strength through dispersion hardening. The Y_2O_3 is more effective than the predominant strengthening phase γ' as a barrier to dislocation motion at 1000 °C or higher. The Y_2O_3 dispersoid does not go into solution in the matrix up to the solidus temperature, and also stabilizes recrystallized grain structure.

MA 754 is manufactured as hot-rolled and solution-annealed flat bar. Thermomechanical processing is employed to create a stable, recrystallized coarse grain structure elongated in the direction of hot working. Grain length to grain width aspect ratios of up to 10 are typical. The highly directional structure leads to varying degrees of anisotropy in mechanical and physical properties. MA 754 has a long $\langle 1\,0\,0 \rangle$ crystallographic texture in the direction parallel to the hot-working direction. The preferred texture results in a low modulus of elasticity in the longitudinal direction and thereby improves resistance to thermal fatigue by lowering the stresses for given thermal strains [5]. In addition, MA 754 shows good stability against high-temperature cyclic oxidation, due to the Ni–Cr composition and the added adhesion of the chromium oxide scale due to the homogeneous distribution of the Y_2O_3 dispersoid [6, 7]. The properties of the alloy have made it desirable for many high-temperature applications (for example, turbine vanes and blades for the F-404 engine, which powers the F-18 fighter plane [8]) which often require joining.

0022–2461

TABLE I Nominal chemical composition of MA 754 (wt %)

Nickel	78
Chromium	20
Aluminium	0.3
Titanium	0.5
Carbon	0.05
Iron	1.0
Yttrium oxide (Y_2O_3)	0.6

TABLE II Physical properties of MA 754

Density ($kg\,m^{-3}$)	8300
Melting point (K)	1673
Lattice parameter (nm)	0.355
Thermal coefficient of expansion ($\times 10^{-6}\,K^{-1}$)	12.22
Specific heat ($J\,kg^{-1}\,K^{-1}$)	440
Thermal conductivity ($W\,m^{-1}\,K^{-1}$)	14.26
Modulus of elasticity (textured) (GPa)	149
Modulus of elasticity (untextured) (GPa)	203

Development of a suitable joining technology is essential for ODS alloys because components with complicated cooling design, such as blades and vanes as well as combustion chambers, cannot be made by other methods. Additionally, optimum utilization of ODS alloys requires joints between sections of the alloy or dissimilar materials because long cross-sections are not available. The joints must exhibit properties suitable for service but must be produced without degrading the properties of the ODS alloys. Excessive heating of the ODS alloys can cause oxide coalescence leading to severe agglomeration, so that the dispersoid may no longer be effective in pinning the dislocations [9]. Melting the ODS alloys results in "slagging off" of the oxide dispersoid so that it is no longer available for strengthening [10]. Melting and resolidification produces an equiaxed grain structure as well as a grain-boundary orientation perpendicular to the directional base-metal grain structure, both of which cause a plane of weakness in the weld. Since most ODS alloys derive much of their strength from an elongated grain structure [3], the disruption of the grain structure results in reduced properties. Thus, development of procedures for joining these materials offers a unique challenge to the welding engineer. Welding by conventional processes, however, has not been successful, since the nature of most welding processes is to melt and resolidify the base metal. The molten pool produced by most welding processes allows the low-density Y_2O_3 to rise to the top of the molten pool and form a slag or be rejected from the solidifying front and agglomerate [11]. Currently, diffusion bonding and hot-isostatic-pressing (HIP) are employed to produce joints in ODS alloys in order to preserve the stress rupture properties.

High energy beam processes using electron beams and lasers can be considered for joining ODS alloys. Since the concentrated energy of these processes melts a minimum of base metal, better-quality weldments than those produced by conventional welding processes, e.g. gas–metal arc welding (MIG) and tungsten-inert-gas welding (TIG), can be expected. In this paper we report the effects of laser welding on the microstructures, mechanical properties and hot corrosion of MA 754 alloy.

2. Experimental procedure

2.1. Material preparation

The material used in this study was a hot-rolled MA 754 alloy with a coarse grain structure (Fig. 1). The microstructure of this alloy consists of spherical Y_2O_3 particles of the order of 0.05 μm in diameter in an fcc Ni–Cr matrix. The Y_2O_3 particles, due to their small size, are not apparent. Inclusions such as yttrium aluminium oxide and titanium carbonitride in the form of small and large dark particles, respectively, are also present and are readily seen. Microtwins and stacking faults are also commonly observed in the microstructures (but not shown in Fig. 1). Welding coupons with a thickness of 3.2 mm (1/8 in.) were machined from a wrought bar of 38.1 mm (1.5 in.) thick. Square grooves were then prepared for butt joining.

2.2. Laser welding

A 1.5 kW continuous-wave CO_2 gas transport laser (Spectra Physics model 820) was used for welding. The output beam size was 19 mm with a Gaussian energy distribution (TEM_{00}). The laser beam was circularly

Figure 1 Optical micrograph showing the grain structure of wrought MA 754 alloy.

polarized and was incident normal to the specimen surface. A ZnSe lens with a focal length of 190 mm (7.5 in.) was used as focusing optics. The specimens were mounted on an $X-Y$ table, the motion of which was controlled by a computer numerical controller. A single laser pass was made on both sides to achieve full penetration in the butt joint. Autogeneous welds were made with a laser power of 1.5 kW and a travel speed of 42.3 mm s^{-1} (100 i.p.m.). The laser beam was focused 0.25 mm below the surface of the specimen. The joint gap was held less than 0.16 mm. Helium was used as the shield gas at about 157 $cm^3 s^{-1}$ during laser irradiation. The welding direction was the same as that of the longitudinal direction of the rolled bar.

2.3. TIG arc welding

TIG welds were made using a filler metal prepared by sectioning a portion of the wrought metal received. The size of filler metal was approximately 3 mm square bar. Welds were made with argon shielding gas and with settings of the a.c. current 0.4 A and the voltage 500 V, and the joint gap was held less than 1 mm. Two overlapping weld passes on both the top and bottom of the workpiece were performed. Weldments were cooled in water immediately after welding.

2.4. Mechanical properties evaluation

Room-temperature tensile and hardness tests were performed on base metal and laser and TIG weldments. For tensile tests, an Instron testing machine with a crosshead speed of 4.2 μm s^{-1} and a load cell capacity of 2000 lb (907 kg) was used in an air environment. The specimens were machined and cleaned with acetone prior to test. Hardness was determined using a Vickers microhardness tester at a load of 500 g.

2.5. Hot-corrosion test

The crucible test described by Steinmetz *et al.* [12] was employed for the hot-corrosion resistance studies of base metal, laser and TIG weldments (Fig. 2). In this test, the specimen is completely or partly submerged in a container of fused salt such as Na_2SO_4 or Na_2SO_4–NaCl mixture at an elevated temperature. Gases may be added through the melt or passed over it to provide oxidizing or reducing environments. Further variations may include successive dipping and removing the specimen from the melt. Because of its simplicity and because the attack is rapid and severe, corrosion mechanisms differing significantly from those prevailing in service conditions can be achieved in the crucible test. The extent of attack may be determined from the depth of penetration of corrosion into the metal.

In order to reduce the aggressiveness and improve the representation by the test of actual service environments, we modified the test configuration. The specimen was first coated with the Na_2SO_4–NaCl salt and then briefly immersed (0.5–1.0 s) in a 25% aqueous Na_2SO_4–NaCl solution. The specimen was then kept for 10 h in a furnace at 900 °C while partially immersed in the solution. Specimens were ground and polished prior to the hot-corrosion tests.

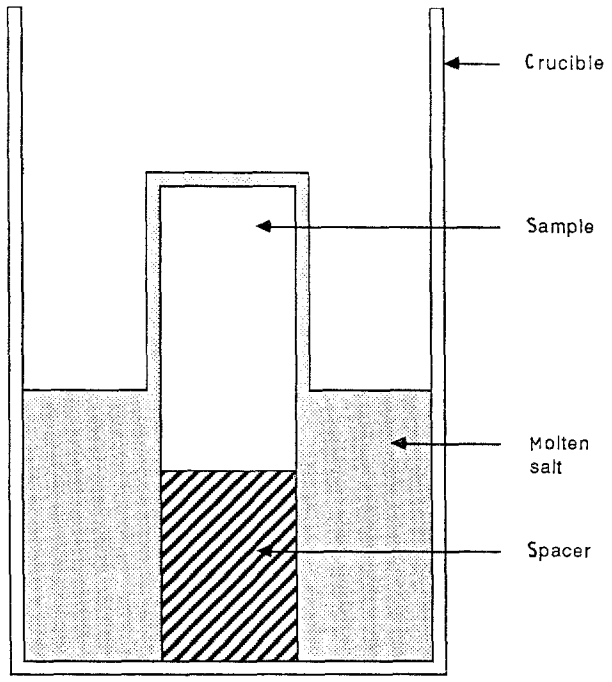

Figure 2 Experimental arrangement for crucible "hot corrosion" test.

2.6. Metallography

Following welding, the fusion zone and base metal of the weldments were prepared for metallographic observation by standard techniques. The welded specimens were etched by 3 parts H_2O, 2 parts HCl and 1 part H_2O_2 to show the general microstructure. A high-resolution optical microscope was used to identify the microstructures. A scanning electron microscope (SEM) was used to examine tensile fractured surfaces. X-ray diffraction using a Siemans diffractometer with CuK_α radiation was used to identify the microstructures.

3. Results and discussion

Fig. 3 shows typical transverse sections of laser-welded MA 754 alloy. There is no evidence of cracks or porosity in the fusion and heat-affected zones. The fusion zone is characterized by a depth-to-width ratio greater than unity. The shape of the fusion zone indicates that a "keyhole" welding mechanism was operative during laser welding. The solidification microstructure of the laser weldment (Fig. 3b) is due to the epitaxial growth from the side-walls of the cavity that produced grain boundaries almost perpendicular to the grain orientation of the base metal. At the centre of the weld fusion zone there is a narrow region where the grain growth is parallel to the base metal grain structure (see also Fig. 5a below). The grain orientation of the weld is an important consideration in determining the weld properties. Ideally, welding should be done such that the grain orientation of the weld and the base metal should be the

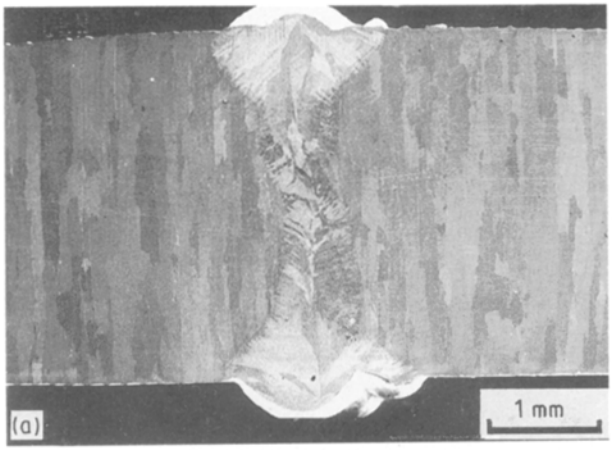

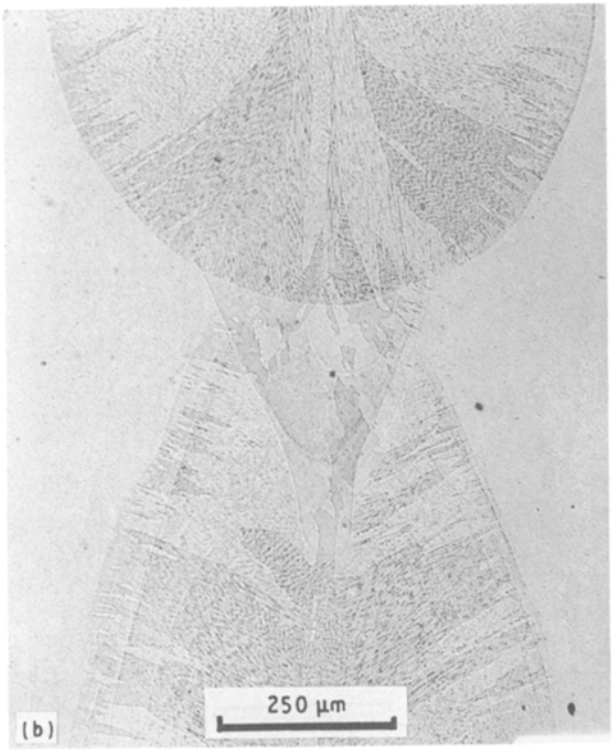

Figure 3 (a) SEM of transverse section showing laser weldment. (b) Optical micrograph showing solidification structure of laser-weld fusion zone.

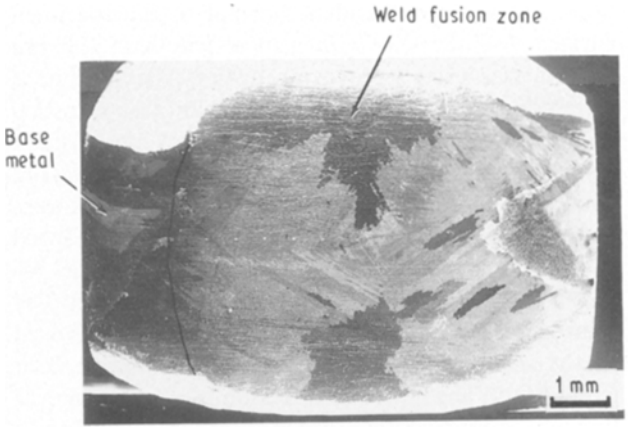

Figure 4 SEM showing one-half of TIG-weld fusion zone.

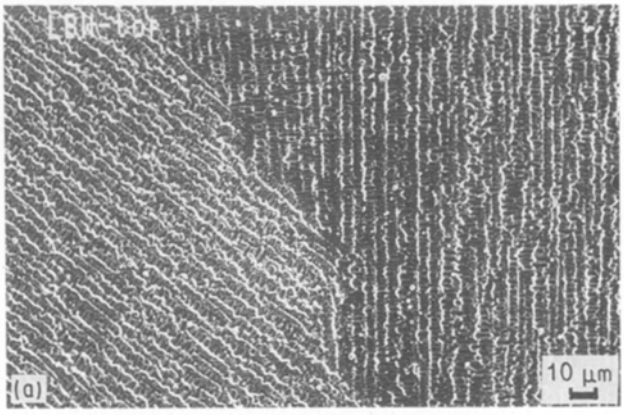

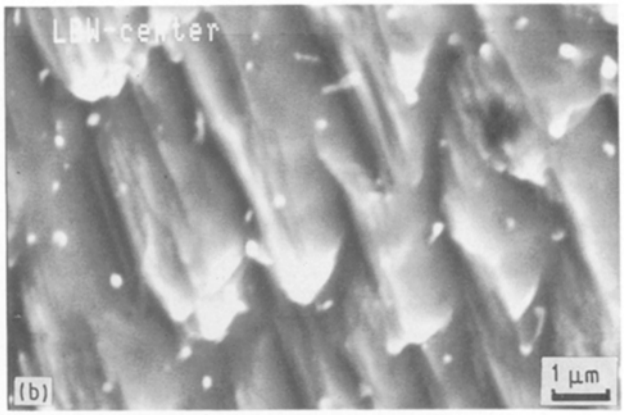

Figure 5 (a) SEM of laser-weld fusion zone showing the centre-line grain growth parallel to the longitudinal grains of the base metal. (b) SEM showing the Y_2O_3 particles in laser-weld fusion zone.

same. It is possible, although we have not attempted it in this study, that orienting the laser beam at some angle to the base-metal grain structure during welding should allow the grains to grow parallel to the grain orientation of the base metal.

Fig. 4 is a transverse section of TIG-welded MA 754 alloy showing the base metal and one-half of the weld. The weld width of TIG weldment is considerably larger (about 14 mm) than that of laser weldment (1.5 mm). The solidification structure is predominantly dendritic with severe micro-segregation. The grain structure consists of equiaxed grains.

Figs 5 and 6 are SEM micrographs showing the microstructures of laser and TIG weldments, respectively. The microstructure of laser weldment consists of Y_2O_3 particles of the order of 0.1 to 0.4 μm in a nichrome matrix. The average particle size of Y_2O_3 is larger in the laser weldment than in the base metal, partly due to Ostwald ripening and partly due to some agglomeration caused by the melting. In the case of the TIG weldment, severe agglomeration of Y_2O_3 particles resulting in an average size of 3 μm can be readily seen. Additionally, there is a significant loss of Y_2O_3 particles observed in the TIG weld, possibly due to the "slagging out". The severe agglomeration in the TIG weld is attributed to the large volume of base metal being melted and resolidified, causing the Y_2O_3 to form slag or be rejected from the solidifying front to

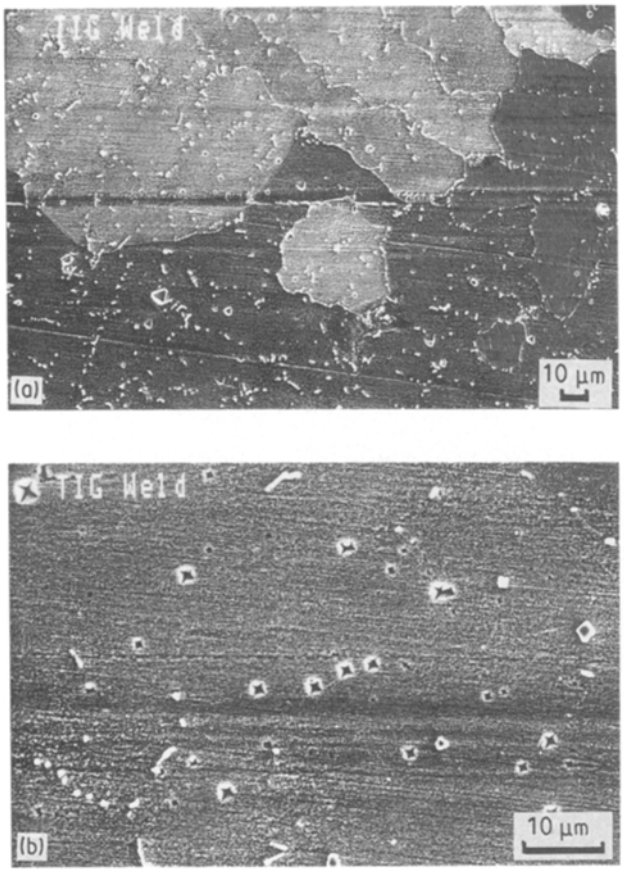

Figure 6 SEM showing the microstructure of the fusion zone of TIG weldment. Note the presence of agglomerated oxides.

form aggregates. The absence of severe agglomeration in laser welding is due to two reasons: lasers are capable of purifying and redistributing the Y_2O_3 particles to a finer degree because such particles absorb more laser energy than the surrounding metal; the high travel speed and highly concentrated energy source of the laser beam would cause a small volume fraction of the base metal to be melted. This is also consistent with the observations by others [10, 13] that the smaller the volume of ODS alloys liquified, the less severe was the oxide agglomeration. A study of pulsed Nd–YAG laser welding of an iron-based ODS alloy MA 956 showed that the oxide dispersoid remained without agglomeration and without "floating out" of the fusion zone [11]. Transmission electron microscopy analysis revealed that the average dispersoid had grown from 0.05 to 0.19 μm in diameter [11].

Fig. 7a to c are the X-ray diffraction patterns of base metal and weldments. The crystallographic textures of weldments differ from that of the base metal as a result of the solidification. Laser weldment exhibits predominantly ⟨2 0 0⟩ growth while TIG weldment has a preferential growth of ⟨2 2 0⟩. In contrast, the base metal shows a strong peak at ⟨1 1 1⟩ in the X-ray pattern.

Textural features contribute to the mechanical properties of a material. A hardness traverse across the width of weldments is shown in Fig. 8a and b. The average hardness in the fusion zone of the laser weldment is lower than that of the base metal but is

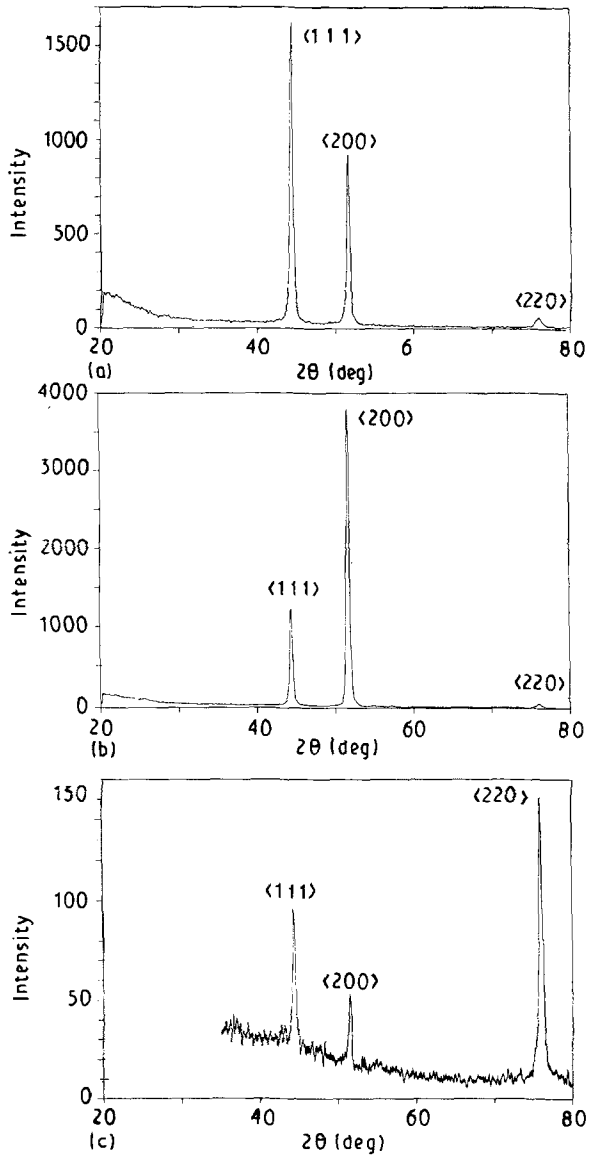

Figure 7 X-ray diffraction patterns of (a) wrought base metal, (b) laser weldment, (c) TIG weldment.

substantially higher than that of the TIG weldment. However, the heat-affected zone of laser weldment exhibited a higher hardness than the base metal. Fig. 9 shows the engineering stress–strain curves of the base metal and the weldments. Table III lists the tensile properties obtained from Fig. 9. It is seen that laser weldment has a better ductility than the base metal and TIG weldment. However, the strength properties (yield and ultimate tensile) of laser weldment are slightly inferior to those of the base metal but substantially higher than that of the TIG weldment.

Both hardness and uniaxial tensile test data indicate the potential of laser welding over arc welding for ODS alloys. The factors that are responsible for the weldment properties include: grain size, extent of agglomeration, grain orientation and texture. In laser weldment, the grain size is small due to rapid solidification and thereby enables an increase in hardness and strength as well as ductility. However, the dispersion hardening mechanism is less effective for the laser weldment than for the base metal because of the coarsening of the oxide. Furthermore, the grain and

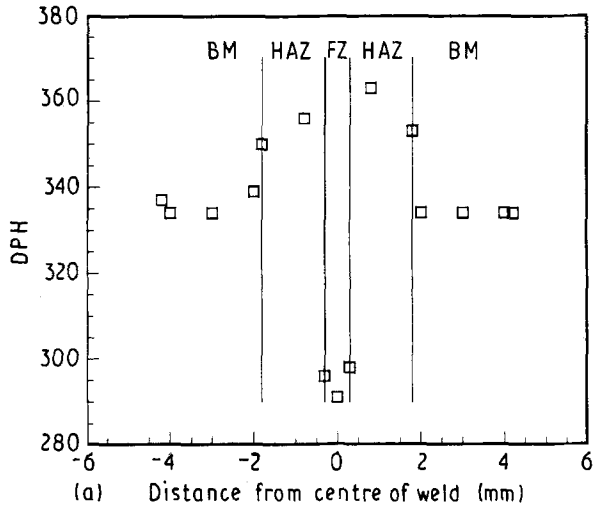

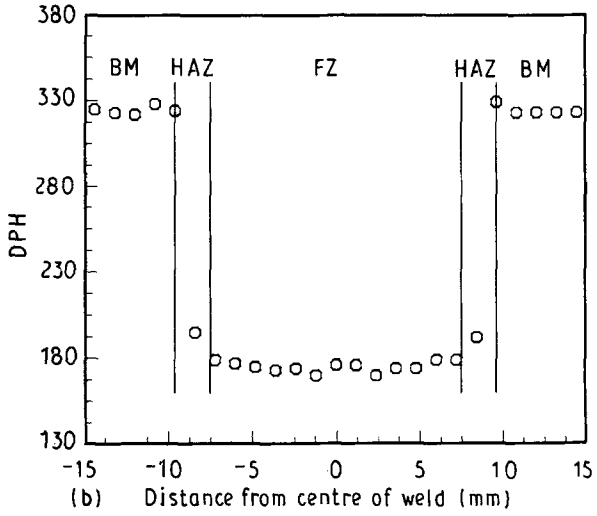

Figure 8 Hardness traverse (DPH, load 500 g) along the width of weldments: (a) laser weldment, (b) TIG weldment. FZ = fusion zone, HAZ = heat-affected zone, BM = base metal.

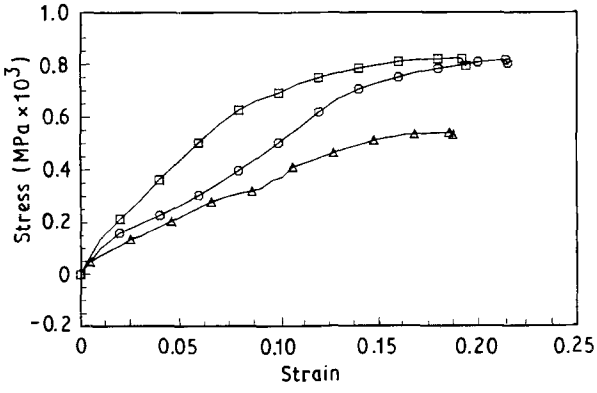

Figure 9 Room-temperature engineering stress–strain curves of wrought metal and weldments: (□) base metal, (○) laser weldment, (△) TIG weldment.

crystal orientations reduce the strength properties. In spite of such deleterious effects, the strength properties of laser weldment are comparable to those of the base metal. Additionally, laser welding can be made to grow the grains parallel to the base-metal grain structure, in which case the strength of laser weldment can

TABLE III Comparison of tensile properties of base metal, laser weldment and TIG weldment

Specimen	Base	Laser	TIG
Yield strength (MPa)	656	620	360
Ultimate strength (MPa)	824	816	540
Elongation (%)	19	22	19
Area reduction (%)	16	18	16

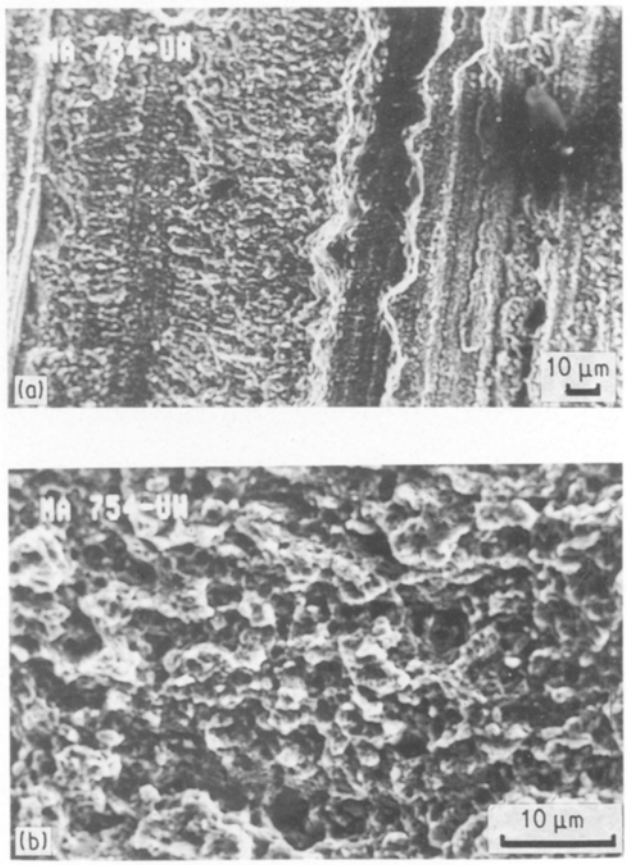

Figure 10 Scanning electron fractographs showing the fracture appearance of wrought MA 754 alloy.

be equal to or better than that of the base metal. The most favourable effect of laser welding is the enhanced ductility.

Figs 10 and 11 show the tensile fracture surfaces of the base metal and the laser weldment, respectively. Large dimples accompanied by ejection of particles can be seen in the tensile fracture of the base metal. In contrast, small dimples distributed uniformly in the fracture zone are visible in the weldment. The size of dimples is governed by the number and distribution of microvoids that are nucleated. In laser weldments, the large number of grain boundaries due to the fine grain size serve as nucleation sites for microvoids. The preferential ⟨200⟩ growth texture and internal stresses due to welding also aid in nucleation of microvoids. Thus laser weldment exhibits an equiaxial arrangement of small dimples and fracture is preceded by the maximum normal stress. The base metal fracture showed elongated dimples indicative of some evidence of shear fracture. Internal plastic deformation might have also distorted the dimple shape. The

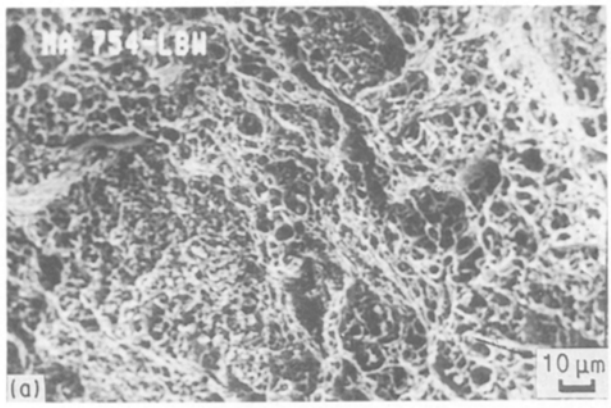

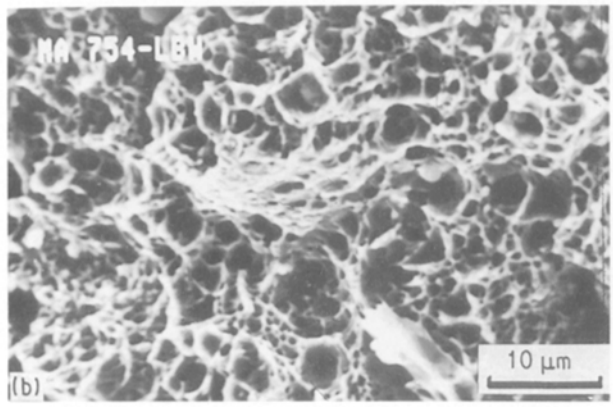

Figure 11 Scanning electron fractographs showing the fracture appearance of laser-welded MA 754 alloy.

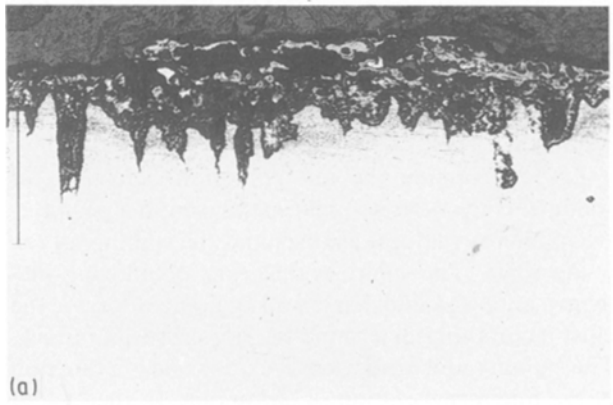

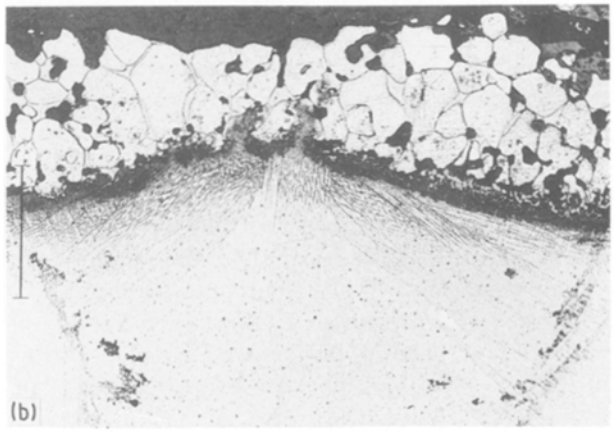

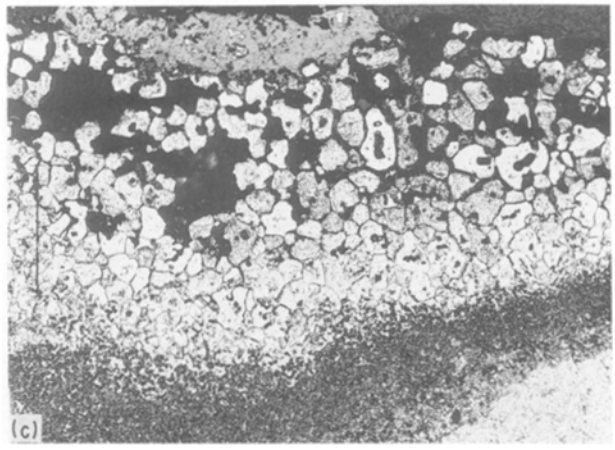

Figure 12 Optical micrographs showing transverse sections of hot-corrosion tested specimens: (a) wrought metal, (b) laser weldment, (c) TIG weldment. (× 72)

differences in grain size, texture, internal stresses and secondary Y_2O_3 phase are thus responsible for the differences in the tensile properties and fracture behaviour of the base metal and the weld.

Hot-corrosion tests showed that the corrosion resistance of laser weldment is inferior to that of the base metal but superior to that of the TIG weldment. Fig. 12a to c shows transverse sections of the corroded areas of the base metal, laser weldment and TIG weldment, respectively. The base metal has a corroded layer of about 125 μm (Fig. 12a) that consists of predominantly oxide scale with minimal sulphur attack. Laser weldment exhibits a corroded layer of about 200 μm thick (Fig. 12b) that is composed of sulphides, oxide scale and some porosity. It should be noted that the centre of the weld has a thin corroded layer as opposed to the ends. There is not much evidence of salt penetration. It is seen in Fig. 12c that TIG weldment has the most severe sulphur attack, of the order of 350 μm. The corroded layer consists of voids and oxides near the surface followed by a deep penetration of sulphide salts leading to catastrophic attack.

Hot corrosion is a form of accelerated oxidation and sulphidation. Hot corrosion occurs in two stages: first, an initiation stage where a protective oxide scale, predominantly Cr_2O_3, is formed by selective oxidation because of the affinity of Cr to O_2 rather than S. Then a film of Na_2SO_4 is deposited on the oxide scale. Second, a propagation stage where a severe attack on the alloy takes place by reaction of the oxide scale with the liquid salt deposit. In the propagation stage, the oxide scale grows while at the same time there is a diffusion of S into the alloy. The oxide reacts with Na_2SO_4 to form Na_2CrO_4. The sulphur released through this reaction diffuses through the dense and compact Cr_2O_3 scale. Oxide depletion occurs and causes less protectiveness, permitting a faster rate of oxidation. Na_2SO_4 penetrates the oxide scale and causes a severe attack on the metal. Internal oxides and chromium sulphides along with $Ni–Ni_3S_2$ eutectic are usually found in the salt deposits.

In the base metal, the hot corrosion is almost exclusively due to the initiation stage. In the weldments, the protective oxide scale becomes porous and

is therefore susceptible to sulphidation attack. Internal sulphide and oxide particles are frequently found in the weldments. However, the degree of propagation stage is less in laser weldment compared to TIG weldment.

Let us examine the hot corrosion behaviour of weldments over the wrought metal from the perspective of microstructural features and the stability of the oxide scale. The micro-segregation of alloying elements, grain size and dispersoid agglomeration are the chief factors that determine the hot corrosion attack. The stability and formation of oxide scale is a function of the micro-segregation of chromium. In the case of wrought base metal, the alloying elements such as Cr are uniformly distributed resulting in the continuous availability of Cr for forming oxide scale. In weldments, there is some segregation in laser weldment due to rapid solidification and much severe segregation in TIG weldment, causing the formation of oxide intermittently. Another factor is the extent of agglomeration of Y_2O_3.

Stringer *et al.* [14] suggested that the dispersoids may be regarded as increasing the rate at which the continuous layer of Cr_2O_3 adjacent to the metal may be formed. This hypothesis is based on the ability of the dispersoid particles in the metal surface to act as nucleation sites for the first-formed oxide, thus decreasing the internuclear spacing. The dispersoids also allow rapid diffusion of chromium along the dispersoid–matrix boundary, resulting in the accelerated lateral growth of Cr_2O_3 nuclei. A decrease in the distance between the adjacent Cr_2O_3 nuclei reduces the time required for the lateral growth process to form a continuous Cr_2O_3. In the case of agglomerated dispersoids found in TIG weldment, these effects become inoperative and hence an increase in corrosion results. Hot-corrosion studies of ODS alloys [15] have indicated that a fine grain size can improve the resistance to hot corrosion attack. Laser weldment was thus less degraded under hot corrosion conditions than TIG weldment due to the fine grain size, less microsegregation and less dispersoid agglomeration.

4. Conclusions

An investigation into the laser and TIG welding behaviour of an ODS Inconel alloy MA 754 was conducted. The principal results and conclusions are:

1. Due to the highly concentrated energy source and fast processing speed, laser beam welding resulted in a small volume fraction of the base metal being melted and resolidified. Lasers are also capable of purifying and redistributing oxides to a finer degree by virtue of the increased absorption of Y_2O_3 dispersoids. As a result, Y_2O_3 dispersoids were not agglomerated. Tungsten-insert-gas (TIG) welding, however, resulted in a large volume of the base metal being melted and resolidified, and thus caused the lighter Y_2O_3 to rise to the top of the molten pool and be rejected from the solidifying front and to form agglomerates.

2. Both laser and TIG welding resulted in a loss of grain orientation. In laser weldment, the loss of grain orientation caused a loss of hardness. In TIG weldment, both oxide agglomeration and loss of grain orientation contributed to the loss of hardness.

3. The yield strength and tensile strength of laser weldments are superior to those of TIG weldments, and are comparable to those of base metal. The ductility properties of laser weldments are better than those of TIG weldment and base metal. The mechanical properties of weldments were explained on the basis of microstructural features and fracture appearance.

4. Hot-corrosion resistances of the base metal and the laser weldment were better than for TIG weldment due to the presence of continuous protective Cr_2O_3 scale layers. TIG weldment suffered from sulphur attacks due to the discontinuous Cr_2O_3 scale caused by the agglomeration of Y_2O_3, microsegregation of alloying elements and the relative coarse grain size.

References

1. G. H. GESSINGER and R. F. SINGER, in "Powder Metallurgy of Superalloys", edited by G. H. Gessinger (Butterworths, London, 1984) pp. 213–292.
2. J. S. BENJAMIN and M. J. BOMFORD, *Metall. Trans.* **5** (1974) 615.
3. J. S. BENJAMIN, *ibid.* **1** (1970) 2943.
4. "Alloy Digest" (Inco Alloys International, London, 1978) Ni-244.
5. "Inco Map" (Inco Alloys International, London, 1978) G1-Cr1.
6. P. S. GILMAN, *Progr. Powder Metall.* **41** (1985) 455.
7. R. C. BENN, in "Micon 86: Optimization of Processing, Properties, and Service Performance Through Microstructural Control", edited by B. L. Bramfitt, R. C. Benn, C. R. Brinkman and G. F. Vander Voort (American Society for Testing and Materials, Philadelphia, 1988) pp. 237–246.
8. L. E. SHOEMAKER, in "Advances in Welding Science and Technology", edited by S. A. David (American Society for Metals, Gatlinburg, TN, 1986) pp. 371–377.
9. T. J. KELLY, "Trends in Welding Research", edited by S. A. David (American Society for Metals, Philadelphia, 1981) pp. 471–487.
10. B. JAHNKE, in "High Temperature Alloys for Gas Turbines and Other Applications I", edited by W. Betz, R. Brunetaud, D. Cousouradis, H. Fishmeister, T. B. Gibbons, I. Kvernes, Y. Lindblom, J. B. Marriott and D. B. Meadowcroft (D. Reidel, Brussels, 1986) pp. 176–216.
11. T. J. KELLY, in Proceedings of Symposium on Laser–Solid Interactions and Laser Processing, Boston, December 1978, Materials Research Society, pp. 215–220.
12. P. STEINMETZ, C. DURET and R. MORBIOLI, *Mater. Sci. Technol.* **2** (1986) 262.
13. T. J. KELLY, in "Frontiers of High Temperature Material I", edited by G. A. Mock (Inco Alloys International, London, 1981) pp. 267–272.
14. J. STRINGER, B. A. WILCOX and R. I. JAFFEE, *Oxid. Met.* **5** (1972) 11.
15. P. HUBER and G. H. GESSINGER, "Materials and Coatings to Resist High Temperature Corrosion" (Applied Science, London, 1978) p. 71.

Received 16 January
and accepted 7 June 1991